Available online at www.sciencedirect.com
ScienceDirect
Acta Materialia 58 (2010) 4650–4659
Acta MATERIALIA
www.elsevier.com/locate/actamat

Surface modeling and chemical solution deposition of $SrO(SrTiO_3)_n$ Ruddlesden–Popper phases

M. Zschornak [a,b,*], S. Gemming [a], E. Gutmann [b], T. Weißbach [b,c], H. Stöcker [b], T. Leisegang [b], T. Riedl [d,e], M. Tränkner [d,e], T. Gemming [d], D.C. Meyer [b,f]

[a] Institut für Ionenstrahlphysik und Materialforschung, FZ Dresden-Rossendorf, D-01314 Dresden, Germany
[b] Institut für Strukturphysik, Technische Universität Dresden, D-01062 Dresden, Germany
[c] Institut für Theoretische Physik, TU Bergakademie Freiberg, D-09596 Freiberg, Germany
[d] IFW Dresden, PF 270116, D-01171 Dresden, Germany
[e] Institut für Werkstoffwissenschaft, Technische Universität Dresden, D-01062 Dresden, Germany
[f] Institut für Experimentelle Physik, TU Bergakademie Freiberg, D-09596 Freiberg, Germany

Received 6 February 2010; received in revised form 19 April 2010; accepted 22 April 2010
Available online 18 May 2010

Abstract

Strontium titanate (STO) is a preferred substrate material for functional oxide growth, whose surface properties can be adjusted through the presence of Ruddlesden–Popper (RP) phases. Here, density functional theory (DFT) is used to model the (1 0 0) and (0 0 1) surfaces of $SrO(SrTiO_3)_n$ RP phases. Relaxed surface structures, electronic properties and stability relations have been determined. In contrast to pure STO, the near-surface SrO–OSr stacking fault can be employed to control surface roughness by adjusting SrO and TiO_2 surface rumpling, to stabilize SrO termination in an SrO-rich surrounding or to increase the band gap in the case of TiO_2 termination. RP thin films have been epitaxially grown on (0 0 1) STO substrates by chemical solution deposition. In agreement with DFT results, the fraction of particular RP phases $n = 1$–3 changes with varying heating rate and molar ratio Sr:Ti. This is discussed in terms of bulk formation energy.

Keywords: Density functional theory; Surface energy; Surface structure; Thin films; Layered structure

1. Introduction

Strontium titanate (STO) is an oxide crystallizing in the perovskite structure at room temperature, exhibiting a phase transition to a tetragonal low-temperature phase at 105 K [1]. Because of its low reactivity, high and strain-dependent dielectric constant [2], large-scale tunability of electric [3,4], dielectric and optical properties [5,6] and a good lattice match with a variety of materials ($a = 3.905$ Å), it is used extensively as a substrate material, e.g. for the growth of ferroelectric thin films [7], ferroelectric tunnel junctions [8], high-T_C superconducting or colossal magnetoresistive films [9,10]. Changes in properties can be induced by dopants, but to some extent they can also be varied within the ternary system Sr–Ti–O by introducing defects. Point defects such as intrinsic oxygen vacancies [4,11–13], line defects such as screw dislocations [14,15] and two-dimensionally extended grain boundaries [16–21] and stacking faults [22–24] change the mechanical, electrical and optical properties of STO. Under Ti-deficient conditions during synthesis, additional SrO planes are introduced as ordered SrO–OSr stacking faults, which occur as Ruddlesden–Popper (RP) phases with a body-centered tetragonal unit cell in the space group $I4/mmm$ [23]. One of the most obvious advantages of these

* Corresponding author at: Institut für Ionenstrahlphysik und Materialforschung, FZ Dresden-Rossendorf, D-01314 Dresden, Germany
E-mail address: matthias.zschornak@physik.tu-dresden.de (M. Zschornak).

1359-6454/$36.00 © 2010 Acta Materialia Inc. Published by Elsevier Ltd. All rights reserved.
doi:10.1016/j.actamat.2010.04.035

defect structures is their structural stability at high temperature [25], which reaches decomposition temperatures above 1600 °C for RP phases with $n = 1$ and 2, although growth of single crystals from the melt is prohibited by peritectic decomposition. Further, they exhibit a strong anisotropy of the dielectric response due to the ordered array of SrO (0 0 1) excess planes [26–29]. Experimental studies of such ordered stacking faults by high-resolution transmission electron microscopy (HRTEM) and wide-angle X-ray diffraction (WAXRD) have been reported (e.g. [30–35]).

Besides ceramic bulk materials or small anisotropic crystals [36] the availability of RP phases in the form of thin films is of particular importance for technical applications. In this context we have lately reported on the oriented growth of $SrO(SrTiO_3)_n$ thin films by chemical solution deposition (CSD) [37]. The applied approach is based on a modified Pechini process, which has been proven also by other authors to be a feasible low-temperature method for the preparation of RP phases [38–40]. Thin films of RP phases have also been prepared following sophisticated layer-by-layer deposition growth techniques realized with molecular beam epitaxy or pulsed-laser deposition setups [32,33,41–43]. More recently, rare-earth doped and thus electrically conducting ceramics and thin films of $SrO(SrTiO_3)_n$, that are promising candidates for thermoelectric energy conversion materials, have been reported [44–46]. An unconventional application of RP phases in adaptive X-ray optics, based on an electric field induced reversible formation of near-surface RP phases in an STO crystal, has been proposed by Meyer et al. [47].

Structural stability as well as electronic, microscopic and elastic properties of STO- and SrO-based layered compounds [48–51] have been theoretically studied within the last decade. Various atomistic simulations, Hartree–Fock (HF) and density functional theory (DFT) calculations are available for RP phases with $n \leqslant 3$, but the stability of the phases has been discussed controversially so far, with respect to both the tendency within the homologous series and their absolute formation energies [31,52,53]. Especially for the formation of the RP phase with $n = 3$, no clear trend could be obtained from previous calculations. Recently the atomistic interactions for larger structures with up to $n = 30$ have been simulated with the classical shell model [54] and an antiferrodistortive ground-state based on an $a^-a^-a^-$ Glazer system of STO was found.

There has been significant research dedicated to the determination of the surface structure and stability of STO, both experimentally [55–57] and by calculation [58–62]. Scanning probe microscopy studies have recently been reviewed by Bonnell and Gara [63]. Herger et al. summarize DFT calculations for TiO_2-terminated surfaces [64]. Extensive reconstructions of different surface terminations have been reported [64–67] for both TiO_2 and SrO terminations. The near-surface SrO–OSr stacking faults, characteristic for RP phases, introduce even more termination variants, which to our knowledge have not been modeled so far. Thus, we study relaxation and energetics of the $SrO(SrTiO_3)_n$ RP surfaces by DFT, aiming at STO surface modifications with a specific variation of surface properties.

Due to the interesting possibilities for the application of RP phases there is a high demand on understanding their stability and energetics as well as their surface properties. Therefore, we investigated the formation process of RP phases using a CSD technique and X-ray diffraction analysis (in Section 2.1). To understand the observations made, theoretical modeling by DFT was employed on the bulk structures (in Section 2.2) and, based thereon, on the surfaces (Section 2.3). Herewith, the stability of certain members of the homologous series is investigated. Their surface properties are evaluated and are discussed in terms of surface structures and electronic properties. Conclusions for dedicated STO surface modifications with a specific variation of surface qualities are given.

2. Materials and methods

2.1. Thin film preparation and characterization methods

Thin films of $SrO(SrTiO_3)_n$ RP phases with $n = 1$–3 have been prepared by CSD via dip coating of (0 0 1) STO substrates from Sr–Ti polymeric precursor solutions followed by three annealing steps for drying, pyrolysis of residual organics and crystallization, respectively. A detailed description of the solution preparation, dip coating procedure and thermal treatment can be found elsewhere [37]. In the present study thin films have been prepared from solutions with two different molar ratios of cations Sr:Ti = 2:1 and 1.75:1, respectively. For heteronucleation at the substrate interface and thus epitaxial growth of crystalline phases in the film, the heating rate for the final crystallization step (hold temperature of 700 °C for a time of 1 h) should play a significant role [68]. Therefore three different heating rates of 15, 20 and 100 K min^{-1} – the latter refers to a rapid thermal annealing realized by direct insertion of the sample into the preheated furnace – were applied. All samples were cooled to room temperature in the furnace at a rate of about 2 K min^{-1}.

WAXRD was applied to examine the phase content in the films after annealing and to clarify the crystallographic orientation relation of RP phases in the film relative to the (0 0 1) STO substrate. Diffraction patterns were recorded in the symmetrically coupled ω–2θ scan mode (with incident angle ω and detection angle 2θ) using an X-ray diffraction system Bruker AXS D8 with secondary Johansson-type graphite monochromator, Cu Kα radiation and scintillation counter. An analysis of diffraction patterns was conducted by comparison with reference data from Powder Diffraction File 2 [69]. For HRTEM, cross-sectional specimens were prepared by the focused ion beam lift-out technique at a final ion energy of 5 keV. The HRTEM investigations were carried out using a FEI Tecnai F30 transmission electron microscope. Simulations of HRTEM images were done using the java version of the EMS software package [70].

2.2. Bulk modeling

For an extended stability discussion according to the formation reaction

$$SrO + n \cdot SrTiO_3 \rightarrow SrO(SrTiO_3)_n \quad (1)$$

and for the calculation of surface energies in the framework of grand canonical thermodynamics, the bulk $SrO(SrTiO_3)_n$ RP homologous series ($n = 0$–5, ∞) has been studied by DFT with the ABINIT code [71]. To assess the influence of the error of the exchange–correlation functional both the generalized-gradient approximation (GGA) with the Perdew–Burke–Ernzerhof functional [72] and the local density approximation (LDA) in Teter–Pade parametrization (TP) [73] were used for comparison in our calculations. Extended norm conserving Teter potentials [74] were employed, which allow for an explicit treatment of semi-core and valence states. We retained the common tetragonal symmetry and did not consider an antiferrodistortive bulk structure, because neither preliminary WAXRD investigations of RP phases [23,37] nor our DFT calculations of an antiferrodistortive STO structure showed a rhombohedral distortion of more than 0.2° ($\alpha = \beta = \gamma = 89.8°$, energy difference <20 meV).

The total energy was converged better than 2.7×10^{-7} eV with a maximum kinetic energy of the plane wave basis set of 823 eV and a k-point grid equivalent to an $8 \times 8 \times 8$ Monkhorst–Pack grid for STO. A small Fermi–Dirac broadening of 0.027 eV (equivalent to 316 K) was applied to facilitate convergence. LDA calculations were carried out for both the body-centered tetragonal and the primitive unit cell. All structures have been fully relaxed with respect to cell geometry and atomic positions up to 2.5×10^{-3} eV Å^{-1}.

2.3. Surface modeling

Experimental studies of CSD prepared thin films with WAXRD and HRTEM reported here show the coexistence of different RP phases stacked along the STO [0 0 1] epitaxial growth direction. Those investigations suggest that different phase sequences between surface and substrate may be obtained depending on the preparation conditions. Studies of such STO–RP interfaces examining interface energy and strain can be found, e.g., in Ref. [31]. Here we focus on the modeling of the surfaces of RP phases with n values of up to $n = 3$ normal to (1 0 0) and (0 0 1). We investigate all possible unreconstructed crystal terminations in a search for the most stable surface structure.

Local DFT calculations were performed with the same parameters as given above and a k-space sampling of 1 point in surface direction. To apply periodic boundary conditions, the supercells for surface calculations comprise a slab of material and sufficient vacuum in surface direction in order to reduce the interaction between periodic replica to less than 1 meV. The number of layers for the slabs was determined by convergence of the surface energy (better than 1 meV); a minimum of 11 oxide layers was found to be necessary for (0 0 1) surface structures. Atomic coordinates were fixed to bulk values for the central atomic plane of the slab between the vacuum layers and all other coordinates were fully relaxed (with remaining force components smaller than 2.5×10^{-3} eV Å^{-1}).

In general, surface energies are positive, because bonds are broken at the surface of the otherwise perfectly coordinated bulk. Surface energies can be calculated by subtracting the total energy of a relaxed bulk structure from the total energy E_{SLAB} of a relaxed surface slab with bulk stoichiometry. Surface energies of non-stoichiometric surfaces can be determined by introducing constituent structures [79], i.e. neighboring phases within the phase diagram, as well as their chemical potentials μ [80]. By those means, the surface energy of a termination can be related to the energy of the reference bulk structure. For the (0 0 1) surfaces of the RP phases studied here, STO and SrO were chosen as constituent structures. Being in equilibrium with the according RP bulk phase and taking into account the stoichiometry of the system the stoichiometrically weighted sum of the chemical potentials has to be equal to the formation energy E_f:

$$\mu_{SrO} + n \cdot \mu_{STO} = E_f = E_{RP} - E_{SrO} - n \cdot E_{STO} \quad (2)$$

As given in Eq. (2), E_f can also be calculated from the difference of the total energies per unit formula of the relaxed bulk structures following Eq. (1). This leaves either μ_{SrO} or μ_{STO} as a free parameter and restricts their equilibrium ranges to $E_f \leqslant \mu_{SrO} \leqslant 0$ and $E_f \leqslant n \cdot \mu_{STO} \leqslant 0$. At the two limits the according RP phase is in equilibrium with either bulk SrO or STO, respectively, and out of the ranges crystallization of the constituents is energetically favorable. The grand canonical potential per surface unit cell (factor 1/2 accounts for two slab surfaces) then reads

$$\Omega = 1/2[E_{SLAB} - N_{SrO}(E_{SrO} + \mu_{SrO}) - N_{STO}(E_{STO} + \mu_{STO})] \quad (3)$$

with N_{SrO} and N_{STO} being the number of corresponding units to form the slab. Applying Eq. (2) and introducing $\mu^r_{SrO} = \mu_{SrO}/E_f$ normalized to the RP formation energy, Eq. (3) can be expressed as

$$\Omega = 1/2[E_{SLAB} - N_{SrO}(E_{SrO} + \mu^r_{SrO} \cdot E_f) - N_{STO}(E_{STO} + 1/n(1 - \mu^r_{SrO}) \cdot E_f)] \quad (4)$$

Thus, by variation of μ^r_{SrO} in the interval [0, 1] the appropriate equilibrium condition with the environment can be applied and the correction with respect to the RP formation energy can be weighted between SrO and STO units.

3. Results and discussion

3.1. Influence of preparation parameters on thin film phase content

First we here describe the results of RP phase formation. As shown in Fig. 1, several members of the RP phases

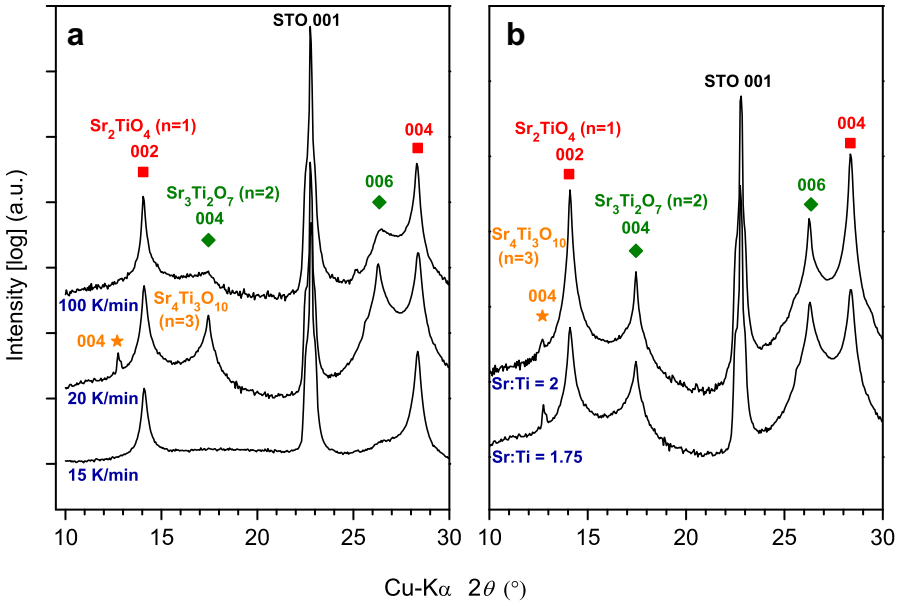

Fig. 1. WAXRD patterns of thin film $SrO(SrTiO_3)_n$ RP phases prepared by CSD under (a) variation of the heating rate of the final annealing step (700 °C, 1 h duration, molar ratio of Sr:Ti = 1.75:1) and (b) variation of the molar ratio Sr:Ti in the precursor solution (heating rate of 20 K min^{-1}).

could be synthesized. It was possible to modify the synthesis parameters such that the phase content could be specifically changed. The influence of selected preparation parameters on the formation of $SrO(SrTiO_3)_n$ RP phases after the final annealing step of 700 °C can be extracted from the WAXRD patterns in Fig. 1. After drying, the films were X-ray amorphous, but already after the second annealing step (pyrolysis of organics) a formation of intermediate crystalline $SrCO_3$ and STO grains was observed in all thin film samples [37]. The present study shows that, besides varying the molar ratio Sr:Ti, the heating rate of the final annealing step alters the fraction of epitaxially grown RP phases with $n = 1$–3 in the films. Neither the duration of annealing nor the cooling rate was observed to affect the phase content in the films. It is well known that in CSD preparation numerous factors, including precursor chemistry, lattice match with the substrate, heating rate and temperature of annealing steps for crystallization and pyrolysis, have a significant effect on film microstructure and orientation (see e.g. Ref. [68] and references therein). In general, a rapid thermal processing is expected to result in highly oriented films, because nucleation is delayed to higher temperatures, thus favoring heterogeneous nucleation at the substrate interface [68]. In the case presented here there is no influence of the heating rate on the orientation of $SrO(SrTiO_3)_n$ films, i.e. highly oriented films can be gained even at relatively low heating rates. This can be attributed to the excellent lattice match of (0 0 1) oriented $SrO(SrTiO_3)_n$ and the (0 0 1) STO substrate, which serves as ideal nucleation site for (0 0 1) oriented grains. This is also underlined by the fact that after a similar annealing schedule of solution prepared powders and films deposited on Si (0 0 1) substrates (having a large lattice mismatch), no RP phases crystallized at all [37].

For films prepared with a molar ratio Sr:Ti = 1.75:1 a slow heating rate of 15 K min^{-1} resulted in the growth of almost solely Sr_2TiO_4, whereas at the higher heating rate of 20 K min^{-1} also oriented grains of $Sr_3Ti_2O_7$ and $Sr_4Ti_3O_{10}$ developed. A rapid thermal processing (heating rate of 100 K min^{-1}) resulted in a preferred growth of both Sr_2TiO_4 and $Sr_3Ti_2O_7$ with a lower volume fraction of the latter phase compared to films annealed with a heating rate of 20 K min^{-1}. Films prepared with a molar ratio Sr:Ti = 2:1 (as in Sr_2TiO_4) and a heating rate of 20 K min^{-1} were not single-phase – also RP members with $n = 2$ and 3 were present – but the fraction of Sr_2TiO_4 was higher compared with films prepared with the smaller molar ratio. Concerning the influence of the heating rate on the volume fraction of competing RP phases, we propose the following interpretation: since the molar ratio Sr:Ti of 1.75:1 in the films lies in between the stoichiometries of the RP phases $n = 1$ and $n = 2$, a coexistence of both phases can be expected. From the viewpoint of bulk formation energies the RP phases with $n = 2$ and 3 should be favored compared to $n = 1$, if their formation energy increases (see Section 3.2). Furthermore, a higher heating rate implies a higher mobility of constituents in the films during the nucleation process. This is suggested to be the reason for a preferred growth of RP phases $n = 2$ and $n = 3$ in the films annealed at increased heating rates of 20 and 100 K min^{-1}, although the effect is less pronounced at 100 K min^{-1}, implying that other factors have to be taken into account, too.

TEM investigations of the film microstructure revealed that the films are not homogeneously crystallized. Amorphous regions and pores were identified between the heteronucleated grains of RP phases, indicating that the hold temperature of 700 °C is slightly too low for a complete crystallization of the film [81]. Besides TEM investigations of the

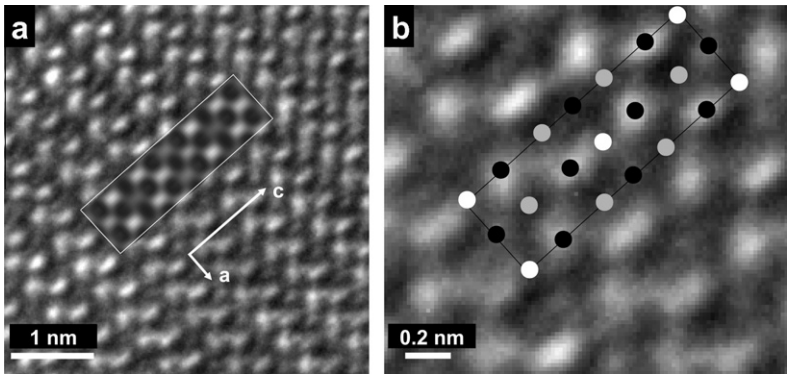

Fig. 2. HRTEM image near Scherzer defocus of an RP phase $n = 1$ film cross-section with an inset (white frame) corresponding to a simulation (a). From comparison of experimental and simulated data the position of the atomic columns (Ti–O in white, Sr in gray, and O in black) can be obtained as shown in the magnification (b).

microstructure and the local chemistry, HRTEM images of RP phases were also recorded. Fig. 2a shows an experimental HRTEM image of the RP phase $n = 1$ with a simulated inset (marked by the white frame). A comparison of the HRTEM simulation with the experimental data reveals the position of the atomic columns as sketched in Fig. 2b. The HRTEM image simulation considers the most important parameters defocus and specimen thickness to match the experimental image. Further experimental details like a mis-tilt of the specimen lead to slight variations of the contrast pattern, but do not change the periodicity which defines the RP phase.

In summary, for a more thorough understanding of cation stoichiometry and heating rate dependence further studies including intermediate heating rates, higher hold temperatures for crystallization and variation of molar ratio of Sr:Ti are necessary.

3.2. Bulk structure modeling

Before the surface properties have been evaluated, the reference RP bulk structures $n = 0$–5, ∞ have been investigated. As presented in Table 1, cell parameters of the relaxed structures agree excellently with our WAXRD results [37] and tabulated experimental data [23], as well as with comparable TEM studies, e.g. Ref. [34]. The deviations amount to less than 0.3% for GGA calculations. Atomic positions differ less than 0.18% on average (max 0.7%). The energies of formation of the homologous RP series from the constituents STO and SrO according to Eq. (1) are shown in Fig. 3 as a function of the SrO–STO ratio. The choice of LDA or GGA exchange–correlation functional and the simulation cell size (body-centered tetragonal or primitive cell) have no effect. We found a gain of formation energy up to the phase $n = 3$, then a saturation threshold at 215 meV is reached, which remains constant for phases of higher order. 150 meV of the total energy gain due to integration of the additional SrO layer is already reached at the phase with $n = 1$, whereas between RP phase $n = 2$ and $n = 3$ the gain further increases by 15 meV. These results imply a consecutive driving force going from phases of lower to higher n up to the RP phase with $n = 3$. They confirm the trends obtained in calculations by Le Bacq et al. [53] but are in general smaller by about 50 meV for both LDA and GGA calculations. Furthermore, these results explain the experimental observations made that the RP phases with $n = 2$ and $n = 3$ occur preferentially at higher heating rates (see Section 3.1). Since we identify a plateau for RP phases with $n > 3$, we can estimate the maximum range of interaction between two neighboring stacking faults to about 11.7 Å. An endothermic formation of the RP phase $n = 3$ [52] or an alternating formation energy within the homologous series [31] could not be confirmed (see Table 2). The difference between DFT and shell model results is typical (see e.g. Refs. [21,16] for grain boundaries), the deviation of the HF results from the general trend may be caused by the complete neglect of differential overlap (CNDO)

Table 1
Cell parameters of the relaxed RP phases with $n = 0$–3, ∞ calculated with LDA and GGA in comparison to tabulated experimental data Exp. [69] as well as results from our measurements [37].

RP	LDA		GGA		Exp.[69]		WAXRD [37]
n	a (Å)	c (Å)	a (Å)	c (Å)	a (Å)	c (Å)	c (Å)
0	5.045	–	5.153	–	5.140 [75]	–	–
1	3.820	12.313	3.892	12.555	3.884 [76]	12.600 [76]	12.571
2	3.838	19.944	3.907	20.306	3.903 [77]	20.372 [77]	20.350
3	3.843	27.587	3.909	28.065	3.900 [23]	28.100 [23]	27.83
∞	3.845	–	3.909	–	3.905 [78]	–	–

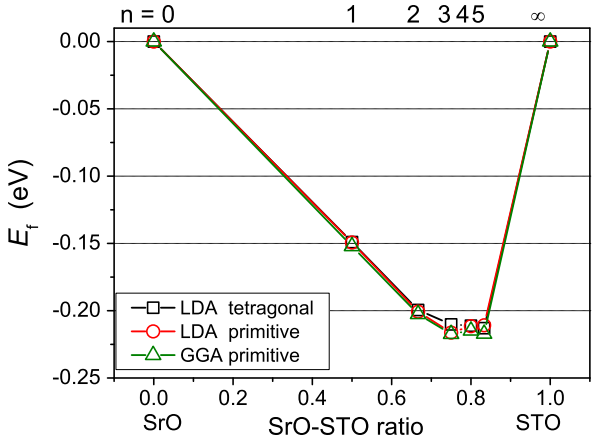

Fig. 3. Calculated energies for the formation of RP phases according to Eq. (1). The integration of the SrO–OSr stacking fault into STO shows exothermic character for all phases and saturates at $n = 3$. Choice of LDA or GGA exchange–correlation functional and unit cell sampling (tetragonal or primitive cell) do not influence the results.

Table 2
Formation energies E_f (eV) from bulk STO and SrO calculated according to Eq. (1) for RP phases with $n = 1$–5 (GGA) compared to other results.

RP n	This work	SM [54] [a]	GGA PW [53]	HF CNDO [52]	SM [31]
1	−0.152	−0.059	−0.200	−0.04	−0.15
2	−0.203	−0.050	−0.252	−0.10	−0.21
3	−0.217	−0.049	−0.269	+0.02	−0.19
4	−0.215	−0.048			
5	−0.217	−0.048			

[a] Most stable of several configurations.

approximation, which is less sensitive to subtle details of the electronic structure.

3.3. Surface modeling

3.3.1. Surface relaxations

From total energy convergence tests the influence of the surface was determined to penetrate into the bulk up to a maximum of two tetragonal unit cells (or about 8 Å) in the [1 0 0] direction within 10 meV and up to five atomic layers (or about 9 Å) in [0 0 1] direction within 1 meV accuracy. The optimized geometries exhibit relaxations of near-surface Ti and Sr atoms towards the interior of the slab, whereas for certain terminations oxygen is pushed out (see Table 3 and the left section of Fig. 4). For the (1 0 0) RP surface with $n = 1$ this relaxation symmetrically distorts the Ti-octahedra along the [1 0 0] direction, while for the RP surface with $n = 2$ additional rotational degrees of freedom within the (0 1 0) plane occur (Fig. 4).

For a comparison of displacement parameters of all modeled (0 0 1) surfaces (schemed in Fig. 5) with reference to the bulk structures we summarize our results in Table 3. In general, within one (0 0 1) or (1 0 0) layer the relaxation of metal atoms away from the bulk position is much larger

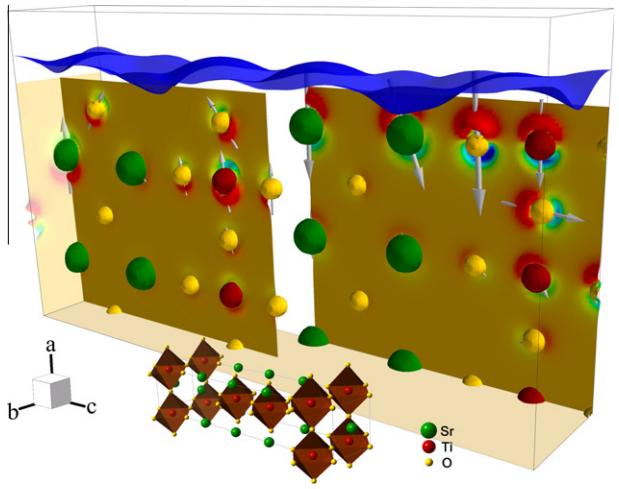

Fig. 4. Two distinct cross-sections of the density difference of valence electrons before (i.e. red maxima) and after surface relaxation (i.e. blue minima) for the RP $n = 2$ (1 0 0) surface (blue). Scaled displacement vectors (square root of length) visualize TiO_6 octahedral distortions and twisting as well as a large atomic displacement where the SrO stacking fault perpendicularly hits the surface (upper center of right section). Isosurfaces of the electron density outline the type of atoms and their relaxed surface positions. The inset shows a unit cell of the structure of the same orientation.

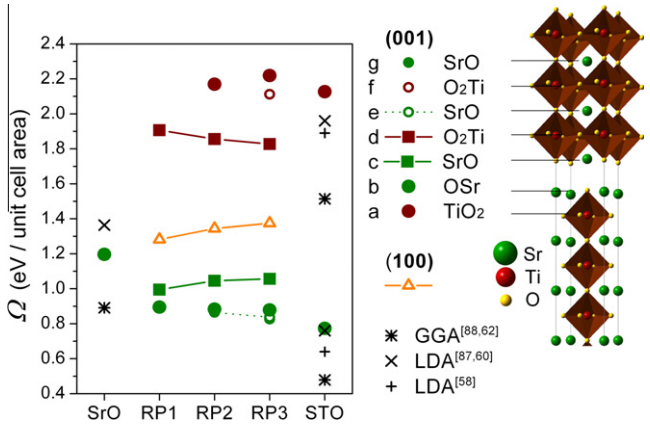

Fig. 5. Grand canonical potential Ω of the RP (1 0 0) and (0 0 1) surfaces of different terminations in SrO-rich surrounding. SrO terminations (green) show in comparison to TiO_2 terminations (brown) smaller surface energies. Configurations with interacting stacking fault (squares) give intermediate values. Reference calculations for SrO and STO surfaces are included.

than the displacement of oxygen atoms of the same layer. Comparing metal atoms of consecutive layers we find a contraction of the surface atoms towards the slab and an alternating sign of the displacements δz for all systems and terminations, with the exception of pure SrO. This is in agreement with results from other calculations of regular STO surfaces (Table 3). The rumpling s of the surface layer describes the absolute distance between metal and oxygen atom in the surface direction and is defined positive when oxygen atoms form the outmost frame of the slab. Rum-

Table 3
Calculated atomic displacements δz of near-surface layers with respect to bulk phases (note: for $n = 1, 2, 3$ layers out of mirror planes have $\Delta z_{Me-O} \neq 0$ in the bulk phase already) and Me–Me interlayer distance changes d_{ij} as a per cent of the bulk lattice constant a_0 next to absolute surface rumpling s in Å compared to experimental data. Positive signs denote displacements towards the slab and rumpling with an outer layer of oxygen. Termination types are labeled according to surface cut sketches in Fig. 5.

n	(0 0 1)	Surface		2nd layer		3rd layer		4th layer		s (10^{-1} Å)	d_{12}	d_{23}
	Conf.	**Sr**/*Ti*	O	**Sr**/*Ti*	O	**Sr**/*Ti*	O	**Sr**/*Ti*	O	Me–O	Me–Me	Me–Me
0	LDA[1]	**0.48**	1.90	**0.03**	−0.60	**−0.04**	0.20	**−0.01**	−0.09	−0.72	−0.45	−0.07
	LDA[2]									−0.64	−1.3[13]	
	GGA[3]	**0.77**	0.96	**−0.96**	−0.39					−0.59	−1.73	0.96
1	a	*4.12*	1.08	**−2.13**	0.79	**0.44**	−0.15	*−0.20*	−0.04	1.17	−6.25	2.58
	b	**0.38**	0.33	*−0.60*	−0.33	**0.21**	−0.06	**−0.05**	0.01	1.79	−0.93	0.81
	c	**1.97**	−0.16	**−0.53**	−0.15	*0.13*	0.01	**−0.15**	−0.04	−0.94	−2.51	0.66
2	a	*3.49*	0.58	**−3.59**	0.21	*0.91*	0.32	**−0.34**	0.23	0.77	−7.08	4.49
	b	**0.54**	0.37	*−0.49*	−0.26	**0.38**	0.00	*−0.08*	0.00	2.15	−1.04	0.87
	c	**2.51**	−0.26	**−0.57**	0.00	*0.25*	0.09	**−0.16**	0.04	−1.02	−3.08	0.82
	d	*3.51*	1.41	**−1.58**	0.83	**0.53**	0.05	*−0.02*	0.10	1.16	−5.09	2.11
	e	**3.92**	−0.83	*−1.47*	−0.32	**0.63**	−0.25	**−0.14**	0.07	1.82	−5.39	2.11
3	a	*2.93*	0.04	**−4.25**	−0.35	*0.39*	−0.18	**−0.92**	−0.20	0.70	−7.18	4.65
	b	**0.44**	0.27	*−0.55*	−0.33	**0.35**	−0.04	*−0.08*	−0.01	2.24	−1.00	0.91
	c	**2.30**	−0.62	**−0.84**	−0.20	*0.06*	−0.10	**−0.32**	−0.12	−1.05	−3.14	0.90
	d	*2.60*	0.63	**−2.23**	0.09	**0.01**	−0.38	*−0.34*	−0.26	1.17	−4.82	2.24
	e	**4.32**	−1.22	*−1.92*	−0.61	**0.52**	−0.53	**−0.29**	−0.02	1.84	−6.24	2.44
	f	*2.51*	0.53	**−3.18**	−0.10	*0.55*	0.12	**−0.43**	0.01	2.17	−5.70	3.73
	g	**4.14**	−0.76	*−1.34*	−0.18	**0.96**	−0.17	*−0.30*	−0.08	0.70	−5.47	2.29
∞	**SrO**[4]	**5.42**	−0.45	*−1.18*	0.15	**1.41**	0.09	*−0.11*	0.14	2.26	−6.60	2.59
	GGA[5]									2.23	−6.96	3.21
	B3[6]	**5.15**	−0.67	*−1.86*	−0.78	**1.22**	−0.01			2.27	−7.01	3.08
	LDA[7]	**6.00**	0.31	*−0.65*	0.47	**1.22**	0.26			2.19	−6.65	1.87
	LDA[8]	**6.63**	−1.02	*−1.79*	−0.26	**1.53**	−0.26	*−0.26*	0.00	3.02	−8.4	3.4
	LDA[9]	**5.70**	−0.10	*−1.19*	0.00	**1.19**	0.10			1.42	−6.9	2.4
	Exp[10]									1.60	2.6	1.3
	Exp[11]									1.6 ± 0.8	−5 ± 1	2 ± 1
	Exp[12]									−0.5 ± 4.7	−0.3 ± 3.6	−6.7 ± 2.8
∞	**TiO_2**[4]	*2.49*	0.72	**−3.05**	−0.06	*0.51*	0.12	**−0.54**	0.01	0.68	−5.54	3.56
	GGA[5]									0.91	−6.81	4.63
	B3[6]	*2.45*	0.27	**−3.59**	−0.38	*0.44*	0.05			0.85	−6.04	4.03
	LDA[7]	*3.22*	1.79	**−2.35**	0.61	*0.64*	0.53			0.55	−5.58	2.99
	LDA[8]	*1.79*	0.26	**−4.59**	−0.77	*0.26*	−0.26	**−1.02**	−0.26	0.71	−6.4	4.7
	LDA[9]	*3.39*	1.61	**−2.51**	0.49	*0.70*	0.49			0.69	−5.9	3.2
	Exp[10]									1.00	1.8	1.3
	Exp[11]									0.8 ± 0.8	1 ± 1	−1 ± 1
	Exp[12]									−5 ± 3.3	0.3 ± 1.0	

Method	a_0 (Å)	Layers	Ref.	Method	a_0 (Å)	Layers	Ref.
[1]LDA TP	5.045	13	This work	[8]LDA CA	3.92	11	[59]
[2]LDA SIC	5.10	8	[87]	[9]LDA PW	3.86	7	[58]
[3]GGA	5.19	7, 9, 11	[88]	[10]RHEED	3.90	(exp.)	[56]
[4]LDA TP	3.845	17	This work	[11]LEED	3.90	(exp.)	[55]
[5]GGA PW	3.94	11	[62]	[12]SXRD	3.905	(exp.)	[57]
[6]hybrid B3PW	3.903	9	[61]	[13]Not Me–Me but average			
[7]LDA	3.85	7	[60]	Bold font: **Sr**, italic font: *Ti*, metal: Me			

pling is found to be negative for the SrO double layer (DL) surfaces and positive for all other configurations. Within the experimental error bars the DFT results agree well with RHEED and LEED analysis of pure STO surfaces listed in Table 3. The apparently contradictory results between experiment and simulation for the distance change d_{12} of the first two metal layers for TiO_2 terminated STO may be attributed to the simplified data refinement model employed for the analysis of the measurements.

Within the homologous RP series, the TiO_2 (SrO) surface rumpling systematically decreases (increases) for higher n and approaches the pure STO limit as the stacking fault is located further away from the surface (configurations a and b, respectively). The rumpling of the SrO–OSr stacking fault termination c, however, is enhanced with an increasing number of STO layers underneath ($n \rightarrow \infty$). For d and e type configurations, representing an STO layer on the SrO DL (in case of $n = 1$ same

configuration as a and b), surface and stacking fault interaction have opposing effects on the atomic displacements, which cause intermediate rumpling values. Higher configurations (f and g) show no significant change compared to pure STO surfaces. These results are in agreement with experimental findings from in situ RHEED analysis of PLD grown RP phases (e.g. Ref. [42]), which report a general roughening and smoothing of the surface during sequential deposition of SrO and STO, respectively.

3.3.2. Density of states

To discuss the electronic structure of different surface terminations in more detail, density of state (DOS) simulations are presented in Fig. 6. The energy range was chosen to cover the first unoccupied states in the conduction band, i.e. titanium 4d and 5s states, and to include the oxygen 2s semi-core states, which can be taken as an indicator for the local mean oxygen crystal potential due to the angle independence of the s states. All surfaces show insulating character, following the experimental [82,83] and theoretical results for pure STO surfaces (e.g. Refs. [58,59,84,85]). In addition, the stacking fault interaction with the surface does not change the conducting behavior. Comparing the DOS characteristics, two strikingly differing features are observed. First, the band gap of TiO_2 terminations is decreased by surface states. This causes a shift of the valence band to lower energies with respect to the values calculated for SrO-terminated slabs and is due to charge redistribution from lone-pair oxygen 2p orbitals of the split Ti-octahedra [86]. For a termination layer neighboring the stacking fault (configuration d), the shift amounts to about 0.5 eV and increases up to 1.0 eV for higher surface–stacking fault distances. Supporting the results from the stability discussions, the ionic SrO terminations show a bulk-like valence band edge without surface states. Second, an energy splitting of the strontium 4p states can be observed exclusively for the stacking fault termination c and may be taken as an indicator for this type of termination. Electron densities in real space have been studied and a comparison between types c and b implies that intraplanar Sr–O bonding gets stronger and more covalent with higher densities between the atoms. This is connected with the large Sr rumpling of the surface layer. Experimentally, this energy splitting might be confirmed with modern photoelectron spectroscopy.

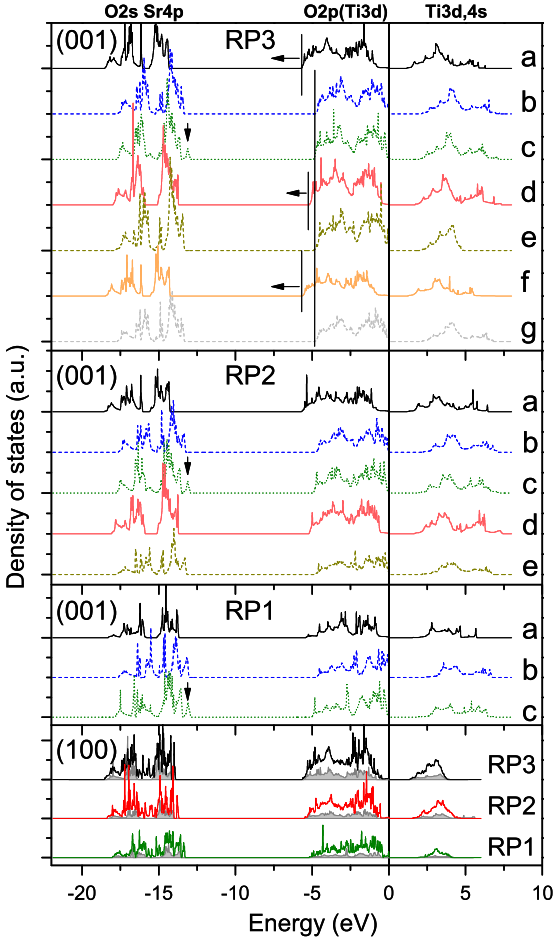

Fig. 6. Density of states of (1 0 0) and (0 0 1) RP surface structures. Solid, dashed and plotted lines indicate TiO_2, SrO and SrO DL configuration types according to surface cuts sketched in Fig. 5. For (1 0 0) plots, the DOS of the bulk RP phases was included in shaded gray. Surface states shift the valence band for TiO_2 terminations which is less effective for a near-surface SrO DL. Additional energy splitting for Sr 4p states is induced by an SrO DL surface (see arrows).

3.3.3. Surface energies

Our studied RP films have been crystallized on STO in a solution of excess SrO, which approaches the limit of $\mu_{SrO} = 0$. A summary of the surface grand canonical potentials calculated following this condition is given in Fig. 5. The examined RP surface cuts are sketched and surface energies per 1×1 unit cell area a_0^2 are shown for all modeled RP phases. Energies are found in an interval of 0.77–2.2 eV per unit cell area. SrO terminations with maximally "buried" stacking fault (green circles) form the energetically most favorable surfaces and their grand canonical potentials approach the value of STO for $n \rightarrow \infty$. The rupture of Ti-octahedra, which occurs for TiO_2 termination (brown circles), costs about 1.3 eV of additional surface energy. Interaction of the stacking fault with the surface reduces the surface grand canonical potential for TiO_2 (brown squares) and increases it for SrO termination (green squares). Since (1 0 0) surfaces are constructed of both SrO and TiO_2 terminations, the energies consistently take intermediate values between the limiting "pure" terminations. The intersection area of the stacking fault, which hits the surface perpendicularly, lowers the surface energy like a stripe of SrO termination and favors RP phases of smaller n, in which SrO-type termination occupies a higher surface fraction.

Considering RP surfaces in thermodynamic equilibrium with a reservoir between the limits of bulk SrO and STO, we calculated the grand canonical potential Ω as a function of the normalized SrO chemical potential μ^r_{SrO} using Eq. (4), as outlined in Section 2.3. The results are summarized in Fig. 7 for all discussed surfaces. SrO and STO precipita-

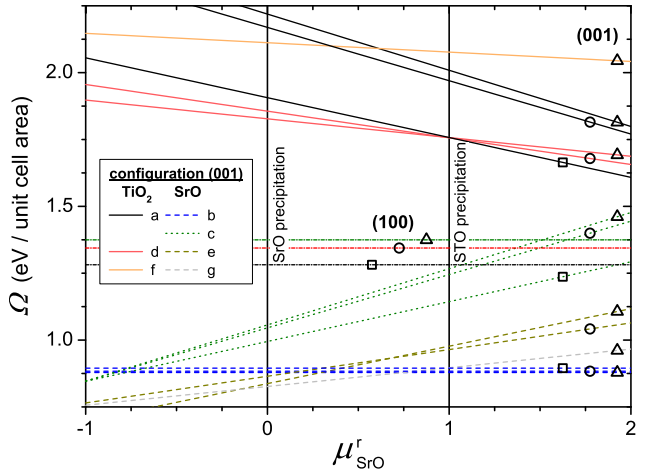

Fig. 7. Calculated grand canonical potential Ω as a function of the normalized chemical potential μ^{r}_{SrO} for all considered types of surfaces. Symbols correspond to the RP phase $n = 1$ (□), 2 (○) and 3 (Δ), respectively. Configuration types a–f are labeled according to surface cut sketches in Fig. 5. The precipitation lines limit the stable equilibrium region out of which SrO and STO crystallites can form, respectively. For SrO terminations in SrO-rich environment a near-surface SrO DL configuration e and g is energetically more favorable than an STO-like configuration b.

tion lines separate the range of RP stability from the regions, where formation of bulk crystallites of SrO or STO is energetically favorable. Stoichiometric terminations such as configuration b (surface cut along the SrO–OSr stacking fault) and (1 0 0) surfaces are invariant under change of the chemical potential. Within the set of SrO terminations the crossing of the grand canonical potential curves of types b, e and g indicates a change of stability relation. Configurations e for RP with $n = 2$ and g for RP with $n = 3$ (inclusion of near-surface SrO DL) are preferred in an SrO-rich surrounding. Configurations b (largest possible SrO DL distance to surface) occur preferentially in an STO-rich environment. TiO_2 terminations a and f with a deeply buried stacking fault exhibit similar changes, whereas terminations with a near-surface SrO–OSr DL (c and d, for $n = 1$ also a) keep their preference order with respect to energy.

4. Conclusions

We have presented a systematic theoretical study of (1 0 0) and (0 0 1) surfaces of $SrO(SrTiO_3)_n$ RP phases with $n = 0, 1, 2, 3, \infty$ and determined optimized structures, electronic properties as well as phase stability relations for all possible unreconstructed crystal terminations. Local density-functional band-structure calculations with a plane-wave pseudopotential code yielded the electronic structure of valence and semi-core states and derived properties. We have shown that the characteristic SrO–OSr stacking fault has significant influence on both surface energies and atomic displacements if it is located close to the surface. In particular, SrO (TiO_2) surface rumpling is decreased (increased), which allows the control of surface roughness in layer deposition growth techniques (e.g. MBE, PLD). Pure STO-like SrO terminations are found to be energetically most stable in STO-rich surrounding, whereas a near-surface SrO–OSr DL is more favorable in contact with an SrO-rich reservoir. The effect of surface states intruding the band gap for TiO_2 termination is decreased by the stacking fault and crystal field splitting of the Sr 4p states is enhanced for an SrO DL surface. In summary, we showed that the vicinity of the RP stacking fault strongly modifies the structure and stability of the surface. This gives rise to a specific and controlled change of surface properties by means of STO near-surface modifications.

From DFT modeling we confirmed a general gain of formation energy for bulk RP phases with increasing n, most significant between $n = 1$ and 2 saturating at $n = 3$. In agreement with this result, thin films of $SrO(SrTiO_3)_n$ RP phases with $n = 1$–3 have been prepared by CSD on (0 0 1) STO substrates starting from Sr–Ti polymeric precursor solutions followed by dip coating and three annealing steps. It was found that variation of the heating rate during the final annealing step and of the molar ratio Sr:Ti alters the fraction of epitaxially grown RP phases with $n = 1$–3 in the films, whereas the orientation of RP phases, grown with the c-direction perpendicular to the perfectly matching (0 0 1) STO substrate, was not influenced. To a certain extent the volume fraction of RP phases present in the films could be discussed in terms of bulk RP phase formation energy but still further studies are necessary for a consistent understanding of the interdependence of preparation parameters and phase formation in these films.

Acknowledgments

This work was funded by the Deutsche Forschungsgemeinschaft (DFG: ME 1433/4-1, GE 1202/5-1, GE 1037/9-2). Furthermore, we would like to express our thanks to Prof. Roger Smith for the careful revision of the manuscript and F. Röder and M. Reibold for stimulating discussions and experimental support.

References

[1] Von Waldkirch T, Müller KA, Berlinger W. Phys Rev B 1973;7:1052.
[2] Antons A, Neaton JB, Rabe KM, Vanderbilt D. Phys Rev B 2005;71:024102.
[3] Hui SQ, Petric A. J Electrochem Soc 2002;149:J1.
[4] Waser R. J Am Ceram Soc 1991;74:1934.
[5] Kulagin N, Dojcilovic J, Popovic D. Cryogenics 2001;41:745.
[6] Hao JH, Luo Z, Gao J. J Appl Phys 2006;100:114107.
[7] Fong DD, Stephenson GB, Streiffer SK, Eastman JA, Auciello O, Fuoss PH, et al. Science 2004;304:1650.
[8] Kohlstedt H, Pertsev NA, Contreras JR, Waser R. Phys Rev B 2005;72:125341.
[9] Kwo J, Hsieh TC, Fleming RM, Hong M, Liou SH, Davidson BA, et al. Phys Rev B 1987;36:4039.
[10] Mitsugi F, Ikegami T, Ebihara K, Narayan J, Grishin AM. Sci Technol Adv Mater 2001;2:525.
[11] Szot K, Speier W, Bihlmayer G, Waser R. Nat Mater 2006;5:312.
[12] Leisegang T, Stöcker H, Levin AA, Weissbach T, Zschornak M, Gutmann E, et al. Phys Rev Lett 2009;102:087601.

[13] Stöcker H, Zschornak M, Leisegang T, Shakhverdova I, Gemming S, Meyer DC. Cryst Res Technol 2010;45:13.
[14] Jia CL, Houben L, Urban K. Phil Mag Lett 2006;86:683.
[15] Brunner D. Acta Mater 2006;54:4999.
[16] Hutt S, Köstlmeier S, Elsässer C. J Phys Condens Matter 2001;13:3949.
[17] Astala R, Bristowe PD. J Phys Condens Matter 2002;14:13635.
[18] Zhang ZL, Sigle W, Phillipp F, Rühle M. Science 2003;302:846.
[19] Zhang ZL, Sigle W, De Souza RA, Kurtz W, Maier J, Rühle M. Acta Mater 2005;53:5007.
[20] Lee SB, Lee JH, Cho YH, Kim DY, Sigle W, Phillipp F, et al. Acta Mater 2008;56:4993.
[21] Benedek NA, Chua ALS, Elsässer C, Sutton AP, Finnis MW. Phys Rev B 2008;78:064110.
[22] Andersson S, Collen B, Kurenteruna U, Magneli A. Acta Chem Scand 1957;11:1641.
[23] Ruddlesden SN, Popper P. Acta Cryst 1957;10:538;
Ruddlesden SN, Popper P. Acta Cryst 1958;11:54.
[24] Benedek NA, Elsässer C, Finnis MW. J Phys Conf Ser 2008;94:012005.
[25] Levin EM, Robbins CR, McMurdie HF. Phase diagrams for ceramists. Columbus, OH: American Ceramic Society; 1964.
[26] Fennie CJ, Rabe KM. Phys Rev B 2003;68:9.
[27] Reshak AH, Auluck S, Kityk I. Jpn J Appl Phys 2008;47:5516.
[28] Orloff ND, Tian W, Fennie CJ, Lee CH, Gu D, Mateu J, et al. Appl Phys Lett 2009;94:3.
[29] Clima S, Pourtois G, Menou N, Popovici M, Rothschild A, Kaczer B, et al. Microelec Eng 2009;86:1936.
[30] Tilley RJD. J Solid State Chem 1977;21:293.
[31] McCoy MA, Grimes RW, Lee WE. Philos Mag A 1997;75:833.
[32] Haeni JH, Theis CD, Schlom DG, Tian W, Pan XQ, Chang H, et al. Appl Phys Lett 2001;78:3292.
[33] Tian W, Pan XQ, Haeni JH, Schlom DG. J Mater Res 2001;16:2013.
[34] Hungria T, MacLaren I, Fuess H, Galy J, Castro A. Mat Lett 2008;62:3095.
[35] Sturm S, Shiojiri M, Ceh M. J Mater Res 2009;24:2596.
[36] Liu YF, Lu YN, Xu M, Zhoun LF. J Am Ceram Soc 2007;90:1774.
[37] Gutmann E, Levin AA, Reibold M, Müller J, Paufler P, Meyer DC. J Solid State Chem 2006;179:1864.
[38] Nishio K, Fukuda K, Imai T, Takenouchi H, Mae H, Fujimoto M, et al. Mat Res Soc Sym Proc 2008;1044:205.
[39] Zhou N, Chen G, Xian HZ, Zhang HJ. Mat Res Bull 2008;43:2554.
[40] Balachandran U, Eror NG. J Mater Sci 1982;17:2133.
[41] Okude M, Ohtomo A, Kita T, Kawasaki M. Appl Phys Exp 2008;1:081201.
[42] Iwazaki Y, Suzuki T, Sekiguchi S, Fujimoto M. Jpn J Appl Phys 1999;38:L1443.
[43] Iwazaki Y, Suzuki T, Sekiguchi S, Fujimoto M. Jpn J Appl Phys 2000;39:L303.
[44] Lee KH, Wang YF, Kim SW, Ohta H, Koumoto K. Int J Appl Ceram Technol 2007;4:326.
[45] Lee KH, Ishizaki A, Kim SW. J Appl Phys 2007;102:033702.
[46] Wang JF, Lee KH, Ohta H, Koumoto K. Ceram Int 2008;34:849.
[47] Meyer DC, Levin AA, Leisegang T, Gutmann E, Paufler P, Reibold M, et al. Appl Phys A 2006;84:31.
[48] Gemming S, Seifert G. Acta Mater 2006;54:4299.
[49] Albina J, Mrovec M, Meyer B, Elsässer C. Phys Rev B 2007;76:165103.
[50] Schwingenschlögl U, Schuster C. Chem Phys Lett 2009;467:354.
[51] Music D, Schneider JM. J Phys Condens Matter 2008;20:055224.
[52] Noguera C. Philos Mag Lett 2000;80:173.
[53] Le Bacq O, Salinas E, Pisch A, Bernard C, Pasturel A. Philos Mag 2006;86:2283.
[54] Freedman DA, Arias TA. arXiv:0901.0157v1 [cond-mat.mtrl-sci]; 2009.
[55] Bickel N, Schmidt G, Heinz K, Müller K. Phys Rev Lett 1989;62:2009.
[56] Hikita T, Hanada T, Kudo M. Surf Sci 1993;287–288:377.
[57] Charlton G, Brennan S, Muryn CA, McGrath R, Norman D, Turner TS, et al. Surf Sci 2000;457:L376–80.
[58] Padilla J, Vanderbilt D. Surf Sci 1998;418:64.
[59] Cheng C, Kunc K, Lee MH. Phys Rev B 2000;62:10409.
[60] Johnston K, Castell MR, Paxton A, Finnis MW. Phys Rev B 2004;70:085415.
[61] Heifets E, Piskunov S, Kotomin EA, Zhukovskii YF, Ellis DE. Phys Rev B 2007;75:115417.
[62] Wang J, Fu M, Wu XS, Bai D. J Appl Phys 2009;105:083526.
[63] Bonnell DA, Garra J. Rep Prog Phys 2008;71:044501.
[64] Herger R, Willmott PR, Bunk O, Schlepuetz CM, Patterson BD, Delley B, et al. Phys Rev B 2007;76:195435.
[65] Erdman N, Poeppelmeier KR, Asta M, Warschkow O, Ellis DE, Marks LD. Nature 2002;419:55.
[66] Lanier CH, Van de Walle A, Erdman N, Landree E, Warschkow O, Kazimirov A, et al. Phys Rev B 2007;76:045421.
[67] Herger R, Willmott PR, Bunk O, Schlepuetz CM, Patterson BD, Delley B. Phys Rev Lett 2007;98:076102.
[68] Schwartz RW, Schneller T, Waser R. C R Chim 2004;7:433.
[69] Powder Diffraction File 2 (PDF-2). Joint Committee on Powder Diffraction Standards – Internation Centre for Diffraction Data (JCPDS-ICDD); 2001.
[70] Stadelmann PA. Ultramicroscopy 1987;21:131.
[71] Gonze X, Beuken JM, Caracas R, Detraux F, Fuchs M, Rignanese GM, et al. Comput Mater Sci 2002;25:478.
[72] Perdew JP, Burke K, Ernzerhof M. Phys Rev Lett 1996;77:3865.
[73] Goedecker S, Teter M, Huetter J. Phys Rev B 1996;54:1703.
[74] Teter M. Phys Rev B 1993;48:5031.
[75] Primak W, Kaufman H, Ward R. J Am Chem Soc 1948;70:2043.
[76] Lukaszewicz K. Angew Chem 1958;70:320.
[77] Elcombe MM, Kisi EH, Hawkins KD, White TJ, Goodman P, Matheson S. Acta Cryst B 1991;47:305.
[78] Nelmes RJ, Meyer GM, Hutton J. Ferroelectrics 1978;21:461.
[79] Padilla J, Vanderbilt D. Phys Rev B 1997;56:1625.
[80] Qian GX, Martin RM, Chadi DJ. Phys Rev B 1988;38:7649.
[81] Riedl T, Gemming T, Weissbach T, Seifert G, Gutmann E, Zschornak M, et al. Ultramicroscopy 2009;110:26.
[82] Henrich VE, Dresselhaus G, Zeiger HJ. Phys Rev B 1978;17:4908.
[83] Chung YW, Weissbard WB. Phys Rev B 1979;20:3456.
[84] Li ZQ, Zhu JL, Wu CQ, Tang Z, Kawazoe Y. Phys Rev B 1998;58:8075.
[85] Piskunov S, Kotomin EA, Heifets E, Maier J, Eglitis RI, Borstel G. Surf Sci 2005;575:75.
[86] Mrovec M, Albina JM, Meyer B, Elsässer C. Phys Rev B 2009;79:245121.
[87] Baumeier B, Krüger P, Pollmann J. Phys Rev B 2007;76:205404.
[88] Skorodumova SV, Hermansson K, Johansson B. Phys Rev B 2005;72:125414.